Mar.2012 / Vol.137

MITSUBISHI ELECTRIC

ADVANCE

Physical Simulation Technology that Supports Our Products

MITSUBISHI ELECTRIC
Changes for the Better

Physical Simulation Technology that Supports Our Products

CONTENTS

Technical Reports

Overview

Author: *Koji Yasui**

Most of Mitsubishi Electric's core products achieve the desired functions based on physical phenomena. These products, such as air conditioning systems, factory automation systems, automotive equipment, elevators, electric power generation equipment, artificial satellites, train control systems, home products, and semiconductor devices, operate based on electrical, mechanical, thermal, and other physical phenomena. These products are expected to provide the answer to market and social demand for lower pricing, energy saving, and higher reliability.

As a tool to meet these requirements, physical simulation technologies become increasingly important. These technologies are continuously evolving and making significant progress; for example, higher speed and accuracy with improved computer performance and wider application areas using new coupled simulation techniques. Mitsubishi Electric uses its leading-edge physical simulation technologies to promote the introduction of new products by reducing the development and design period, and by improving the effectiveness and reliability of new functions. Several interesting examples are presented in this special issue.

*Advanced Technology R&D Center

Simulation Technology for Advanced Laser Processing Machines

Authors: *Junichi Nishimae*, Tatsuya Yamamoto** and *Shuichi Fujikawa**

In the development of laser processing machines, it is important to generate a laser beam suitable for the material to be processed. We have developed a simulation technology for predicting and optimizing the laser beam generated by a laser oscillator, and thus created a sheet metal laser cutting machine with superior cutting performance.

1. Introduction

Laser material processing has become indispensable in many industrial fields. Mitsubishi Electric has released a wide range of laser processing machines for industrial applications such as sheet metal cutting and microdrilling of printed circuit boards, and has been conducting research and development to improve the productivity (processing time), quality and other performances.

An important aspect of the development of laser processing machines is ensuring that the generated laser beam is suitable for the material to be processed. This paper presents the simulation technology used in developing the sheet metal laser cutting machine in order to generate the optimum laser beam for the cutting process.

2. Outline of Sheet Metal Laser Cutting Machine

In the sheet metal laser cutting machine, high-power laser beams are converged and irradiated onto a metal sheet; molten metal generated along the irradiation trace is removed by an assist gas pressure or other means; and thus the metal sheet is cut into the intended shape. As a machine tool that delivers high processing speed not achievable by mechanical processing, and flexibility not achievable by press working, the laser cutting machine is widely used for prototype fabrication and mass production in automotive, electric equipment, and other sheet metal processing areas.

As an example of the sheet metal laser cutting machine, Fig. 1 shows the external appearance of the "ML3015LVP-45CF-R" 2D laser processing machine.[1] The machine consists of a main body, which performs cutting by scanning the converged laser beam along a predetermined path on the metal sheet, and a laser oscillator, which supplies the laser beam to the main body. The laser oscillator for the sheet metal cutting is generally a high-power carbon dioxide (CO_2) gas laser oscillator with an output of 2–6 kW. (The example in Fig. 1 has a laser output of 4.5 kW.)

Figure 2 shows a cutting example of mild steel plates 4.5 to 19 mm in thickness.[2] Free-form cutting with a good cut-surface quality is achieved for a wide range of plate thicknesses not available by press working, and at a much faster speed than mechanical processing.

To achieve the material processing as shown in Fig. 2, which uses laser cutting, it is important to develop an oscillator that generates a laser beam suitable for the material to be processed as well as to develop the required technologies for improving the processing

CO$_2$ laser oscillator: ML45CF-R

SS400: t4.5 – t19mm

Main body of processing machine: ML3015LVP

Fig. 1 2D laser processing machine "ML3015LVP-45CF-R"

Fig. 2 Cutting example of mild steel plates

*Advanced Technology R&D Center
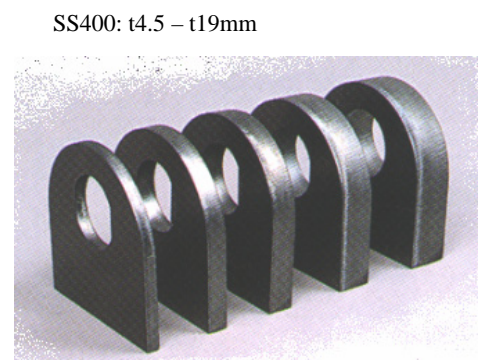
capability, e.g., a machine that enables high-speed and high-precision beam scanning, and optimization of the assist gas for blowing through a nozzle.

Figure 3 shows a conceptual configuration of the CO_2 laser oscillator generating a laser beam.[3] Laser gas, containing CO_2 molecules that emit a laser light, flows between a pair of discharge electrodes; discharge between the electrodes excites the CO_2 molecules, thereby creating a gain medium that amplifies the light. In this configuration, the light travels back and forth in the laser resonator consisting of a total reflector and a partial reflector; the light is amplified by the gain medium, and then emitted through the partial reflector as a laser beam. The operating performance of the CO_2 laser deteriorates with higher temperature of the laser gas; therefore it is cooled by circulation using an axial blower and a heat exchanger. The configuration of the Mitsubishi Electric CO_2 laser is a three-axis orthogonal type, because the three directions of the beam optical axis, gas flow, and discharge current are perpendicular to each other.
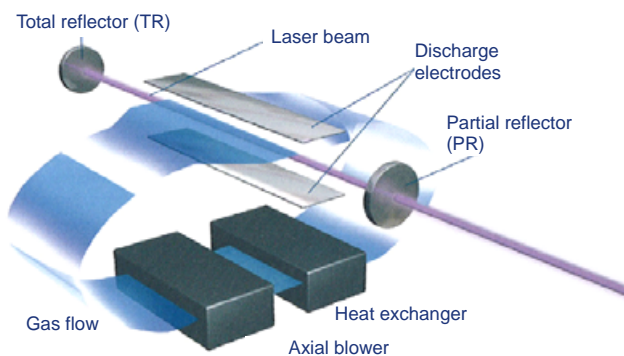
Fig. 3 Conceptual configuration of the three-axis orthogonal CO_2 laser oscillator

To improve the quality of material processing, it is extremely important to optimize the quality of the beam generated by the laser oscillator. In addition to using the optimum mode order, the effect of even a slight difference in the beam profile cannot be ignored. As a higher laser output power has become available for sheet metal cutting, the processable plate thickness and cutting speed have also increased, resulting in stricter quality requirements for the output beam from the oscillator. Meanwhile, as shown in Fig. 3, the beam mode is determined by the discharge excitation, spatial laser beam propagation, and other physical processes coexisting in the CO_2 laser oscillator, and thus it is difficult to accurately predict the quality of the output beam. It takes a significant number of man-hours to determine the equipment parameters through trial and error to generate the optimum laser beam for the material processing. Consequently, to improve the development efficiency, we have produced a technology to simulate how the beam mode is established in the oscillator.

3. Simulation of Beam Mode Creation

In the CO_2 laser oscillator, as described in the previous section, the beam mode is being created while multiple physical phenomena simultaneously occur and influence each other:

- Excitation of CO_2 molecules by discharge plasma
- Transport of the excited molecules by the gas flow
- Interaction between the excited molecules and laser beam (stimulated emission)
- Spatial propagation of the beam between the resonator mirrors

In order to accurately predict the beam mode to be created in the CO_2 laser oscillator, it is necessary to develop mathematical models for all of the abovementioned physical phenomena and computer codes for simultaneous analysis considering their mutual interactions based on the three-axis orthogonal CO_2 laser configuration. Figure 4 shows a block diagram of the simulator developed for creating the beam mode.

To analyze the discharge process, which is the excitation source in the laser oscillator, a discharge simulation based on the Boltzmann equation is used. The Boltzmann analysis is useful for examining the process by which electrons are energized by the electric field and are distributed for the excitation and/or ionization processes that occur during the discharge, and is thus widely used at Mitsubishi Electric for developing ozonizers and other high-performance discharge products.

The Boltzmann analysis provided an excitation efficiency in the laser excitation discharge, optimum gas composition, etc.; the obtained analytical values are compared with the test data for verification and then used in the simulation of the beam mode creation.

The laser oscillation is generated when a laser beam is amplified by the gain medium that has a light amplifying function. The gain medium of the CO_2 laser can be analyzed based on a series of equations called the rate equation, which gives the density of CO_2 molecules in the excited state. The rate equation generally accounts for only time variation; however, Mitsubishi Electric has developed a computer code that can calculate both the time variation and spatial distribution of the gain medium, by considering the configuration of the three-axis orthogonal CO_2 laser and adding the transport effect of CO_2 molecules due to the gas flow.

In the laser oscillator, a beam mode is established while the laser beam is traveling back and forth in the laser resonator, which consists of total and partial reflectors, and being amplified by the gain medium. The beam propagation between the resonator mirrors is calculated by the Fresnel diffraction integral using a fast Fourier transform (FFT) algorithm.

The beam mode to be established in the laser oscillator can be predicted by simultaneously computing the above-described analyses to obtain consistent

states of the laser beam and gain medium. Figure 5 shows an example of the output mode obtained by using the developed simulation code.

The optimum beam mode order for the cutting operation is dependent on the material to be processed. For example, as the thickness of the plate to be cut increases to a certain level, a wide cutting groove must be maintained for removal of the molten metal, and hence the optimum beam mode shifts to a higher order mode. In addition, a slight distortion in the mode geometry or the light on the periphery of the beam, which cannot be described by a simple index such as the mode order, may significantly affect the cutting capability. By using the simulation technology for the beam mode creation, the oscillator's structural parameters can be optimized with the detailed configuration taken into consideration, including the distribution of gain medium, distribution of the laser gas temperature, and optical aperture arrangement that determines the mode. This improves the development efficiency for the oscillators, which are customized in accordance with the materials to be processed and various users' needs, and helps create products with the best cutting speed and cut-surface quality in the industry.

References

(1) Hitoshi Kidokoro and Junji Kano: Mitsubishi Denki Giho, 84 (2010) 151.
(2) Takasi Inoue, Toru Murai, and Masaru Kanaoka: Journal of Japan Laser Processing Society, 13 (2006) 1.
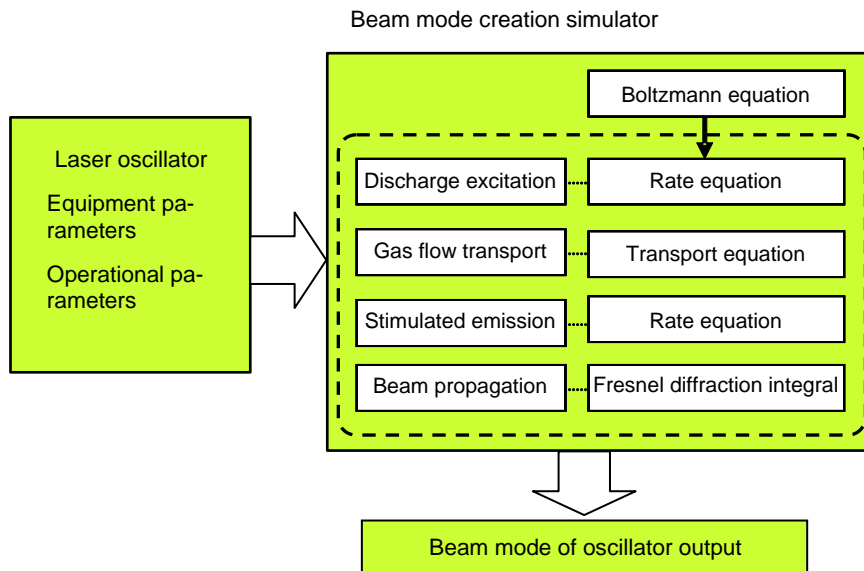(3) Shuichi Fujikawa, Junichi Nishimae, Toru Murai, and Koji Yasui: Review of Laser Engineering, 38 (2010) 160.

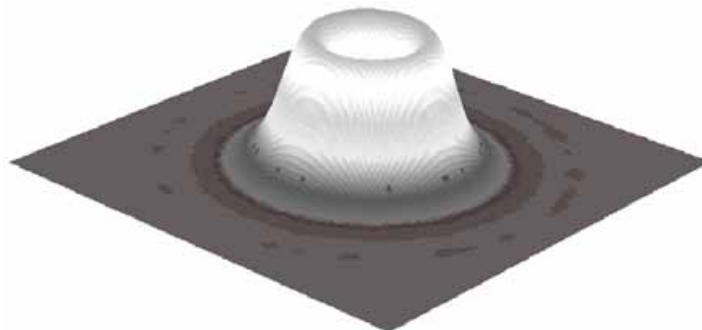Fig. 4 Block diagram of the simulation of beam mode creation

Fig. 5 Calculation example of the output beam mode of the three-axis orthogonal CO_2 laser

Prediction of Resin Flow Direction and Structural Analysis in FRP

Authors: *Hiroo Sakamoto** and *Satoko Baba***

1. Introduction

An increasing number of products are being made from fiber reinforced plastics (FRP) to achieve lower cost, higher stiffness, and higher strength. Generally, molded resins are anisotropic and their elastic modulus, strength, and other mechanical properties differ between the mold direction (MD) and transverse direction (TD). Especially in the case of FRPs, the resin flow direction has a significant influence on the mechanical characteristics,[1] and thus for the structural design of FRP products, it is essential to consider the resin flow direction in the structural analysis.

In order to find the resin flow conditions, a flow analysis is generally performed.[2] However, a software package is required for both flow analysis and structural analysis, and due to different mesh data required by those codes, the results of flow analysis must be mapped to the structural analysis, and hence there are very few examples of structural analysis reported with the resin flow direction taken into consideration.[3]

In this paper, we propose a new structural analysis method using general-purpose structural analysis software, where the flow analysis is substituted by a heat transfer analysis that can be easily coupled with the structural analysis; the resin flow direction is simply approximated by the heat flux direction obtained from the heat transfer analysis; and then in accordance with the obtained resin flow direction, the anisotropic mechanical properties are entered into the structural analysis.

2. Coupling between Prediction of Flow Direction and Structural Analysis

From the fundamental energy equation of thermal fluid, the terms related to the heat transfer analysis are extracted and then simplified for the case of thin-wall-thickness models, yielding a simplified differential equation (1) that governs the heat conduction:

$$\rho c\left(\frac{\partial T}{\partial t}+V_x\frac{\partial T}{\partial x}+V_y\frac{\partial T}{\partial y}\right)=K_z\frac{\partial^2 T}{\partial z^2}+Q \quad \text{.......} \ (1)$$

In the flow analysis for the computer-aided engineering (CAE) of injection molding, the energy equation is simplified in the same manner as Eq. (2):[4]

$$\rho c\left(\frac{\partial T}{\partial t}+V_x\frac{\partial T}{\partial x}+V_y\frac{\partial T}{\partial y}\right)$$
$$=K_z\frac{\partial^2 T}{\partial z^2}+\tau_{xz}\frac{\partial V_x}{\partial z}+\tau_{yz}\frac{\partial V_y}{\partial z}+Q \qquad \text{.......} \ (2)$$

where

ρ : Density [kg/m^3]
C : Specific heat [J/(kg·K)]
T : Temperature [K]
T : Time [s]
V_x, V_y, V_z : Velocity of heat in the conducting medium [m/s]
K_x, K_y, K_z : Thermal conductivity [W/(m·K)]
τ : Shear stress [Pa]
Q : Internal heat generation per unit volume [W/m^3].

A comparison of Eqs. (1) and (2) reveals that the heat transfer analysis does not include the effect of shear stress on the velocity gradient in the direction of the plate thickness in the flow analysis.

Therefore, if the shear stress is negligible, that is, if the viscosity and shear velocity, the determining factors of the shear stress, are negligible, the flow analysis can be simply approximated by the heat transfer analysis. Here, the viscosity is expressed as a function of the shear velocity, temperature and pressure, and thus for simple shapes in which those quantities do not vary greatly, such as those having few resin flow inlets (gates) or little variation in the plate thickness, and an inner volume of molded product that is far from the flow front and/or die wall, heat transfer analysis is considered to be valid in the practical design process for obtaining the resin flow direction, i.e., the ratio between V_x and V_y.

To predict the resin flow direction using the heat transfer analysis code, which is included in the general-purpose structural analysis software, the whole system is set to a certain temperature; a transient thermal analysis is performed after a higher temperature is given to the gate position; the obtained heat flux direction substitutes for the resin flow direction; the mechanical properties in the flow direction are set to the mold direction (MD) mechanical properties and those in the direction perpendicular to it are set to the transverse

direction (TD) properties; and finally, a structural analysis is performed, which provides the results with the resin flow direction taken into consideration.

3. Prediction of Resin Flow Direction in the Propeller Fan and Its Verification

The transient thermal analysis was performed to predict the resin flow direction in the propeller fan using ANSYS 11.0, a general-purpose FEM software package. Figure 1 shows the analysis model. All elements used were of the 10-node tetrahedral solid (Number 87), and the mesh size was set to 3 mm. As the boundary conditions, the temperature was set to 0 at all nodes except for the gate node, where it was set to 1.

Figure 2 shows the distribution of heat flux vectors obtained by the transient thermal analysis. The heat flux spreads from the gate position in the radial direction.

The validity of the predicted resin flow direction was verified by comparing it with the resin flow direction of the actual product. Since the direction of the fiber orientation, on the whole, agrees with the direction of the resin flow [4], the fiber orientation in the propeller fan was observed, instead of the actual resin flow direction in the product, by transmission photography using X-ray computed tomography (CT) equipment (XVA-160CT, UNI-HITE System Corporation). The resulting schematic for the direction of the fiber orientation is shown in Fig. 3. The comparison between the schematic diagram

obtained for the fiber orientation and Fig. 2 indicating the heat flux direction demonstrates that the direction of fiber orientation in the actual product almost matches that of the heat flux direction, confirming the validity of predicting the resin flow direction by heat transfer analysis.

4. Structural Analysis of Propeller Fan and Its Verification

To perform the structural analysis considering the resin flow direction, based on the pre-defined element coordinate system (right-handed orthogonal coordinate system, xyz), the direction of the primary axis (x) of each element is set to align with the heat flux direction obtained by the heat transfer analysis. By doing this, the elastic modulus in the resin flow direction for the structural analysis can be set to the value of the MD elastic modulus.

Table 1 shows the material parameters used for the analysis at the temperature of 20°C. It should be noted that JIS test pieces are used for the experimental evaluation of the elastic modulus and the longitudinal direction of those test pieces is mostly aligned with the resin flow direction, and thus the elastic modulus to be measured is the MD value. Analysis Case 1 assumed isotropic material properties using the elastic modulus measurement of the JIS test piece; Analysis Case 2 assumed anisotropic material properties using the
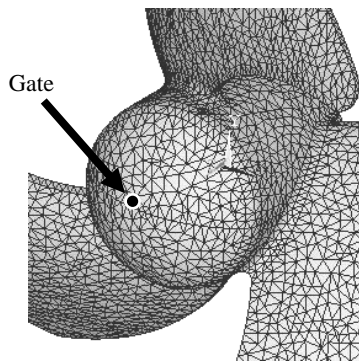
* (54,427 nodes, 27,246 elements)
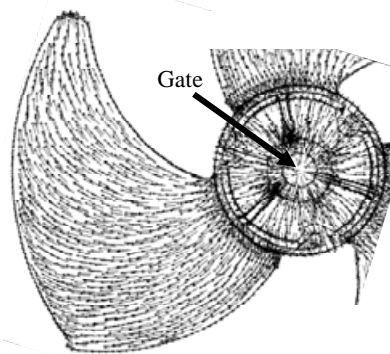
Fig. 1 FEM model
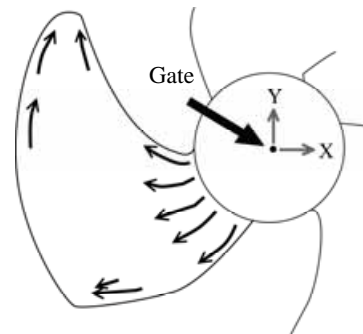

Fig. 2 Distribution of heat flux vectors

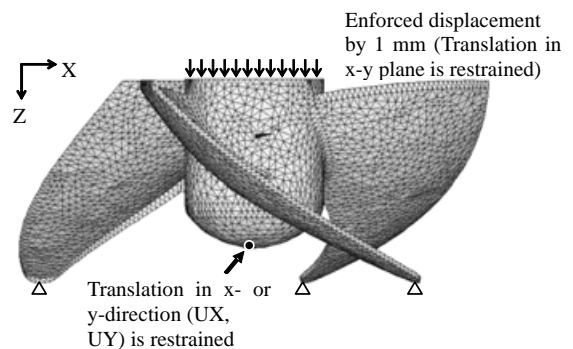Fig. 3 Schematic diagram of the direction of fiber orientation

Fig. 4 Boundary conditions

measurement of the JIS test piece as the MD elastic modulus, and a theoretical value calculated by the rule of mixtures (Ruess model) as the TD elastic modulus.

Table 1 Material parameters

Analysis	Elastic modulus [GPa]		Poisson's ratio	Density [kg/m³]
	MD	TD		
1: Isotropy	3.58		0.35	1040
2: Anisotropy	3.58	1.75		

The 10-node tetrahedral solid element (Number 187) was used. In the static analysis, as shown in Fig. 4, an enforced displacement of 1 mm is given to the end surface of the cylinder in the center of the fan, and the restraint conditions were as follows: at the tips of all blades (3 nodes), translation in the axial (z) direction was restrained; and at the gate position in the center of the model, translation in the x-y plane was restrained. In the eigenvalue analysis, the block Lanczos method was used to obtain the eigenvalues. Using a personal computer with a 3.2 GHz Pentium 4 processor, the time required for the heat transfer analysis and structural analysis was about 2 minutes for the static analysis and about 6 minutes for the eigenvalue analysis.

Figure 5 shows the load versus displacement curves obtained by the analyses and by the compression test under the same simulated conditions. The measurement curve mostly agrees with the results of Analysis Case 2 that considers the resin flow direction, whereas the conventional prediction using the isotropic properties predicts a higher rigidity than that of the actual product.
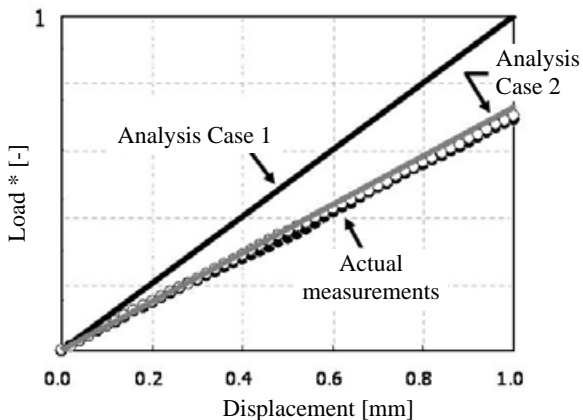

Fig. 5 Comparison of load versus displacement curves (Load is converted to dimensionless quantity by the maximum load of Case 1)

Figure 6 shows the relationship between the analytical eigenvalues and the experimental values obtained by the vibration test on the actual product. The dashed line indicates the condition where the analytical eigenvalue agrees with the actual product. In Analysis

Case 2 considering the resin flow direction, the results show good agreement with the measurements for all modes, whereas in Analysis Case 1 using the isotropic properties, the results differ significantly from the measurements, and moreover, there was no fourth-mode eigenvalue, which appeared in the measurement and the analysis considering the resin flow direction.
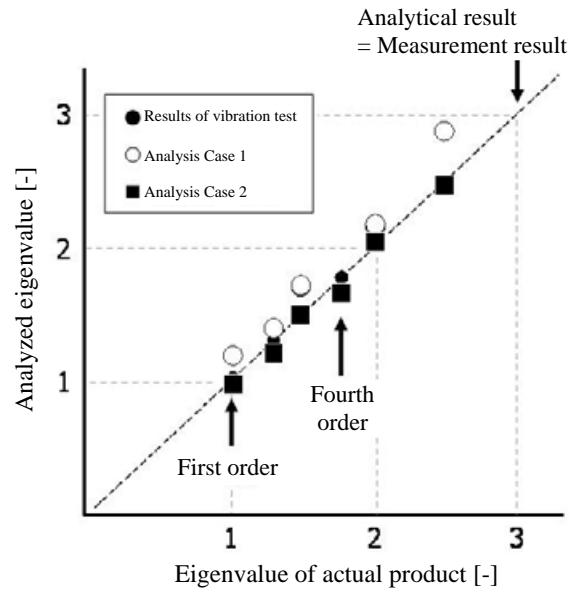

Fig. 6 Comparison of eigenvalues (Converted to dimensionless quantity by the first-order eigenvalue)

5. Conclusion

We have developed and evaluated the validity of a structural analysis method for fiber reinforced plastic products, where the resin flow direction is simply approximated by the heat flux direction predicted by the transfer analysis code, which is included in the general-purpose structural analysis software package; and then in accordance with the obtained resin flow direction, the anisotropic mechanical properties are entered into the analysis. The observation of the fiber orientation using X-ray CT confirmed that the heat flux direction obtained by the heat transfer analysis almost matches the resin flow direction. In addition, the new technique was applied to the static analysis and eigenvalue analysis of the propeller fan, which yielded results showing good agreement between the analysis considering the resin flow direction and the experiments. This technique has improved the precision of the structural analysis for fiber reinforced plastics, and hence provides an optimized gate position, product structure, etc., making it possible to achieve a lighter weight, higher rigidity, greater strength, shorter design period, and better reliability.

References

(1) K. Tohgo et al.: Trans. of JSME, Series A, Vol. 59, No. 557 (1993), pp. 62-67.

(2) S. T. Chung et al.: "Numerical simulation of fiber orientation in injection molding of short-fiber-reinforced thermoplastics," SPE, Vol. 35, No. 7 (1995), pp. 604-618.

(3) Peter H. Foss: "Coupling of flow simulation and structural analysis for glass-filled thermoplastics," Polymer Composites, Vol. 25, No. 4 (2004), pp. 343-354.

(4) H.S. Hele-Shaw: Trans. of the Institute of Architecture, Vol. 11, No. 25 (1989).

(5) R. Nakano et al.: "Fiber Orientation Observation by X-ray CT and Simulation," J. of JSPP, Vol. 20, No. 4 (2008), pp. 237-241.

Natural Frequency Calculation Tool for Turbo-Generator Stator Coil End

Author: *Yoichi Tamiya**

This paper describes the development of a support tool for the vibration design of the turbo-generator stator coil end. This tool easily generates a finite element method model of a stator coil end having a complex structure, and automatically performs the natural frequency calculation and outputs the results. This tool is already used in the actual design process of stator coil ends.

1. Introduction

The turbo-generator stator coil end is excited at a frequency twice the rotating frequency by the electromagnetic force during power generation. If the stator coil end resonates at this frequency, the electric insulation of the stator coil will break down. Thus, appropriate vibration design is essential to prevent resonance.

In recent years, dramatic improvements in computer performance have made it possible to use analysis by the finite element method (FEM) for the vibration design of stator coil ends.[1-3] FEM is an indispensable tool for the vibration design of stator coil ends. However, the stator coil end has an extremely complex structure, as shown in Fig. 1, and hence requires a huge amount of time and sophisticated computer aided engineering (CAE) techniques to create an FEM model and perform the calculations.

The design support tool presented in this paper enables easy and rapid parameter studies such as structural parameter modifications. This tool adopts the ANSYS Parametric Design Language (APDL)[4] of the finite element analysis software ANSYS. The APDL is a programming language written only with ANSYS command terms to automatically create an FEM model, perform calculation and output the results.

2. Support Structure of Stator Coil End

Figure 2 illustrates two types of support structures of the stator coil end: a resin cone type and a resin ring type. In the resin cone type, the stator coil is held between the resin cones and a segment plate and then is tightened with insulation bolts to maintain strong cylinder rigidity. In the resin ring type, the upper coils, lower coils, and coil supports are tied to the resin ring with fiber reinforced plastic (FRP) bands to maintain cylinder rigidity.
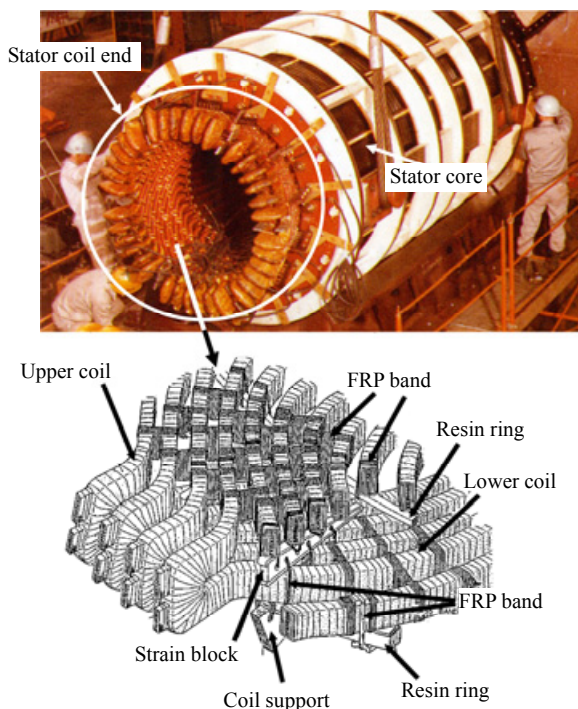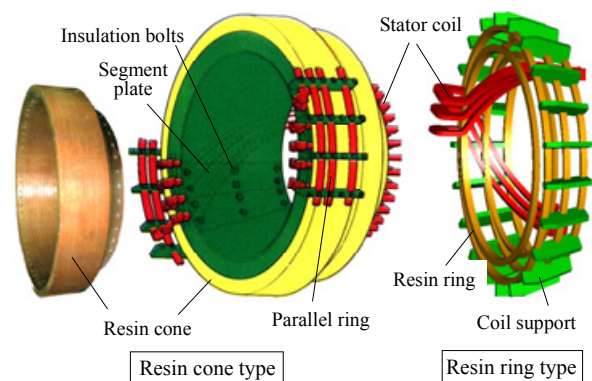

Fig. 2 Support structure of a stator coil end

3. Natural Frequency Calculation Tool for Stator Coil End

The overview of this tool will briefly be described. In this tool, the key dimensions of the stator core and stator coil end are entered in a Microsoft Excel table of dimensions; an APDL file is created and output by an Excel macro function in text file format; ANSYS is started and the APDL file is read in; and then the FEM model is created, calculated, and the results output automatically.

Fig. 1 Structure of a stator coil end

*Advanced Technology R&D Center

The key dimensions of the stator core and stator coil end to be entered into the Excel sheet include: the stator core's inner and outer diameters, the number of slots, cross-sectional dimensions of the stator coil, coil end length, resin ring dimensions, and resin cone dimensions. The design engineer is able to easily create an FEM model using this dimensional information.

Figure 3 shows both the resin ring type and resin cone type FEM models created by this tool for the stator coil ends. This tool can create FEM models for slot counts from 30 to 78 every three slots, and thus can also model two-pole and four-pole machines.
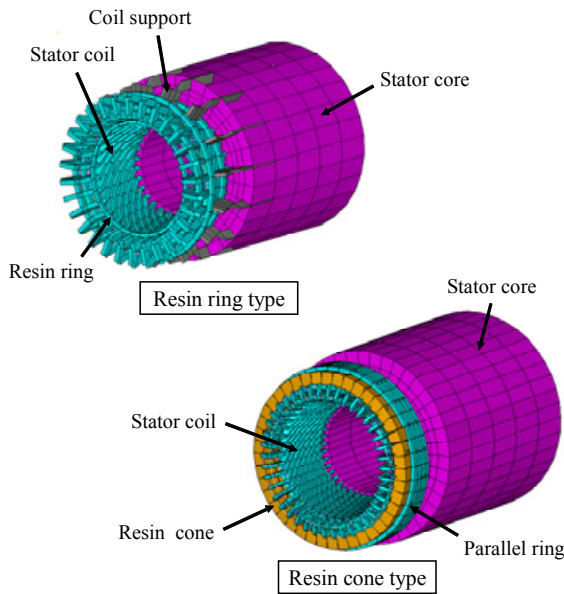
Fig. 3 FEM model of a stator coil end

In the FEM models shown in Fig. 3, the stator core is modeled with solid elements; the resin cone and coil end support with shell elements; the stator coil, resin ring, and phase ring with beam elements; and the FRP tying band with spring elements. If all the structures are modeled using only solid elements having many nodes, the computation time would be huge. Therefore, we worked out a way to use the shell, bar and spring elements to keep the total number of nodes less than 8,000 in this modeling.

4. Natural Frequency Calculation Results for Stator Coil End

Figure 4 shows the correlation between the natural frequencies of the turbo-generator stator coil end obtained by the modal impact test and those by the FEM analysis. Figures 4 (a) and (b) show the correlation results for five of the resin ring type and six of the resin cone type models, respectively. All five resin ring models are two-pole machines. For the resin cone type, five of the six models are two-pole machines and one model is a four-pole machine.

In Fig. 4, for all four modal shapes, i.e., two-node

Modal shape	2-pole
2 node	◆
4 node	●
6 node	▲
8 node	■

Modal shape	2-pole	4-pole
2 node	◆	-
4 node	●	○
6 node	▲	△
8 node	-	□
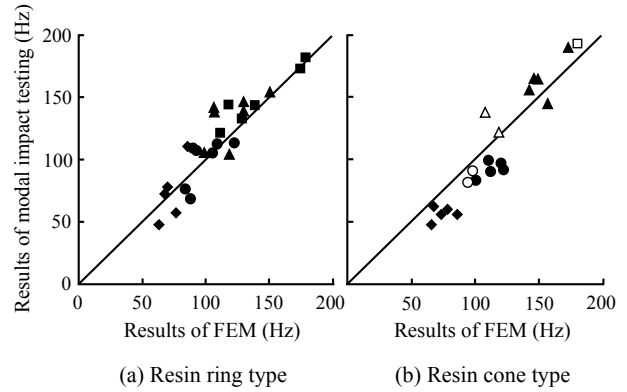
Fig. 4 Correlation of the natural frequency between modal impact testing and FEM

(a) Resin ring type (b) Resin cone type

mode, four-node mode, six-node mode and eight-node mode, the modal impact test and FEM analysis results show good agreement with each other. These results confirm the validity of this FEM modeling for the stator coil ends, and the usefulness of this tool for designing the stator coil end to avoid resonance. The four model shapes: two-node, four-node, six-node, and eight-node modes, are depicted in Fig. 5, which are the shapes of the stator coil end seen from the axial direction of the turbo-generator.
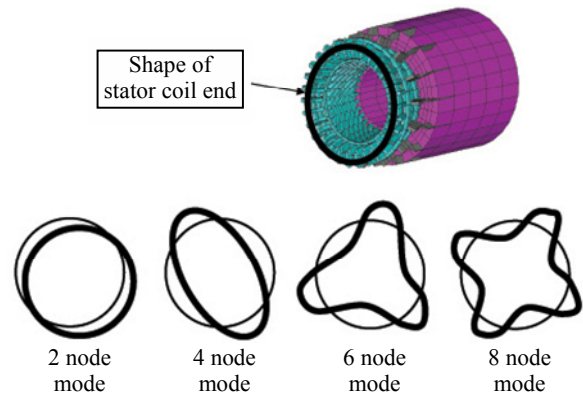
Fig. 5 Modal shape of a stator coil end

5. Conclusion

This paper presented a tool that easily generates an FEM model of the stator coil end having a complex structure, and automatically performs the natural frequency calculation and output of the results. This tool makes it possible to easily and rapidly perform the vibration design of the turbo-generator stator coil end and is already used in the actual design process of stator coil ends.

References

(1) Stephan, C. E., et al.: New air-cooled turbogenerator in the 300-MVA class, ABB Review, No. 1, 20-28 (1996).

(2) Senske, K., et al.: Vibrational Behaviour of the Turbo-generator Stator End Winding in Case of Electrical Failures, CIGRE SC11 IEE Japan (1997).

(3) Shinohara, K., et al.: Natural Vibration Characteristics of a Stator Coil End of a Turbine Generator, Transactions of the Japan Society of Mechanical Engineers Series C, Vol. 70, No. 692, 941-948 (2004).

(4) Cyber Net: ANSYS APDL Guide (2007).

Motor Design Technologies Considering Deteriorated Magnetic Properties in Magnetic Core Due to Stamping

Authors: *Shinichi Yamaguchi** and *Akihiro Daikoku**

1. Introduction

Along with saving energy and resources of the devices for global environmental protection, it is necessary to design low-loss, compact motors. This requires an accurate understanding of the magnetic properties of the iron core in a mass-produced motor. Mitsubishi Electric has been developing design technologies taking into consideration the magnetic anisotropy of iron cores, and the stress conditions arising from the shrink fitting process.[1] In the process of mass-producing motors, iron cores are generally fabricated by press stamping an electric steel sheet. In the stamping process, strain is generated in the iron core material near the sheared edge surface and residual stress remains in a wide area; the effect from the strain and stress causes deterioration of the magnetic properties of the iron core of the motor. However, it was conventionally impossible to quantitatively determine how the deteriorated magnetic properties affected the motor performance. This paper describes a new analysis technique that provides an accurate understanding, at the design stage, of how the stamping process affects the motor performance, and presents the results of analysis on an example case of the permanent magnet motor.

2. Motor Design Considering Deteriorated Magnetic Properties Due to Stamping Process [2]

The analysis system considering deterioration due to the stamping process consists of the following four subsystems:

(1) Measurement of the magnetic properties of the iron core raw material to which strain and stress have been applied.
(2) Analysis of the stamping process for the motor iron core, and calculation of the amount of strain and stress inside the iron core after the stamping process.
(3) Based on the database of iron core magnetic properties and the results of stamping analysis, generation of input data for the magnetic analysis.
(4) Linkage between the generated mesh data with the material property numbers and BH characteristics curve to carry out the magnetic analysis. The stress value is set to von Mises stress, which is suitable for evaluating a metal material.

3. Magnetic Properties of Electric Steel Sheet under Strain and Stress

To measure the magnetic properties of an electric steel sheet under strain and stress, a test sample was stretched to apply a strain of 0 to 15%. Magnetic measurement was performed using a single sheet tester capable of applying the stress. Figure 1 shows an example measurement of the magnetic properties under the strain and stress. Figure 1(a) shows the BH curves under 0% or 5% plastic strain and compressive stress; Fig. 1(b) shows iron loss versus applied stress
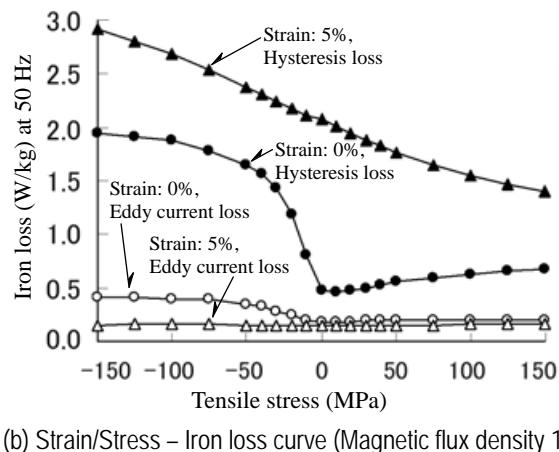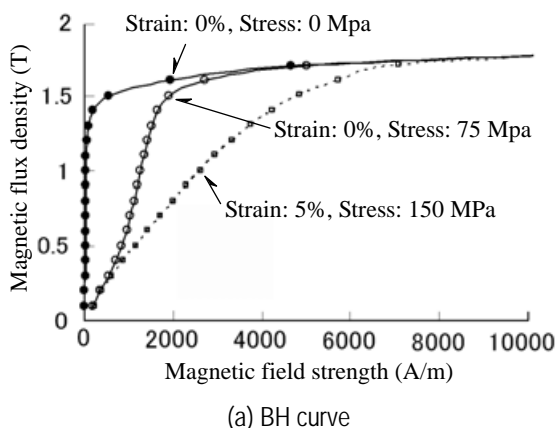

(a) BH curve

(b) Strain/Stress – Iron loss curve (Magnetic flux density 1 T)

Fig. 1 Measured results of the magnetic characteristics of magnetic steel with applied strain and stress

Advanced Technology R&D Center

(magnetic flux density: 1 T). These measurement results indicate that the BH curve changes under the strain and/or stress; and the strain and stress have a significant influence on the hysteresis loss, which increases as the amount of strain and compressive stress increases.

4. Motor for Verification and Analysis Results

Figure 2 shows a cross-sectional view of the motor used for the verification. The motor was a permanent magnet motor with eight poles and twelve slots. This paper discusses the effect of the stamping process on the basic performance of the permanent magnet motor: cogging torque and no-load iron loss.

Assuming that the stator iron core would be made by stamping an electric steel sheet, the stamping process was examined through structural analysis. Figure 3 shows the analysis results of the stress and strain versus the distance from the sheared edge of the iron core at the tooth center. The figure indicates that high strain and stress exist in the vicinity of the sheared edge, distributed within about half the thickness of the electric steel sheet.
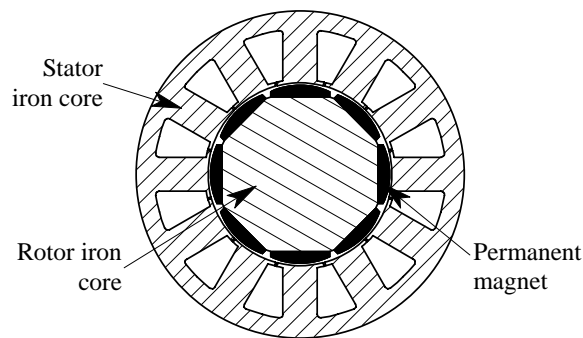
Figure 4 shows the mesh data for the magnetic analysis taking into consideration the strain and stress obtained by the stamping analysis. The shade level of each element in the model indicates the material property number corresponding to different magnetic properties, which is assigned according to each strain value and stress value. Using the mesh data in Fig. 4 and the measurement data of the magnetic properties versus the amount of strain and stress in Fig. 1, the cogging torque and iron loss were calculated by magnetic analysis, yielding the results shown in Fig. 5. It should be noted that the iron loss, W, is expressed as the sum of the eddy current loss, W_e, and the hysteresis loss, W_h, and thus is calculated by the following equation:

$$W = W_e + W_h$$
$$= \sum_m \left\{ K_e(\varepsilon, \sigma) B^{\alpha(\varepsilon, \sigma)} f^{\gamma(\varepsilon, \sigma)} + K_h(\varepsilon, \sigma) B^{\beta(\varepsilon, \sigma)} f \right\} \rho$$

$$\cdots\cdots (1)$$

where K_e, K_h, α, β, and γ are the functions of the strain ε and stress σ, which were identified from the iron loss measurements in Fig. 1; f is the frequency, ρ is the density of the electric steel sheet, and m is the element number in the mesh data. The operating conditions for
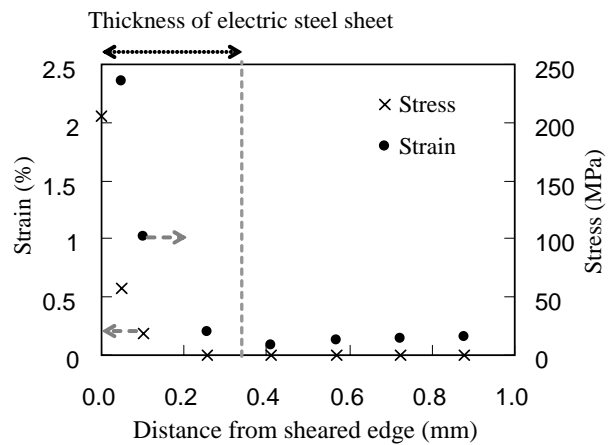

Fig. 2 Verification model

Fig. 3 Calculated results of stress value and strain value versus distance from the edge of the core at the center of a tooth

(a) Tooth of a motor core

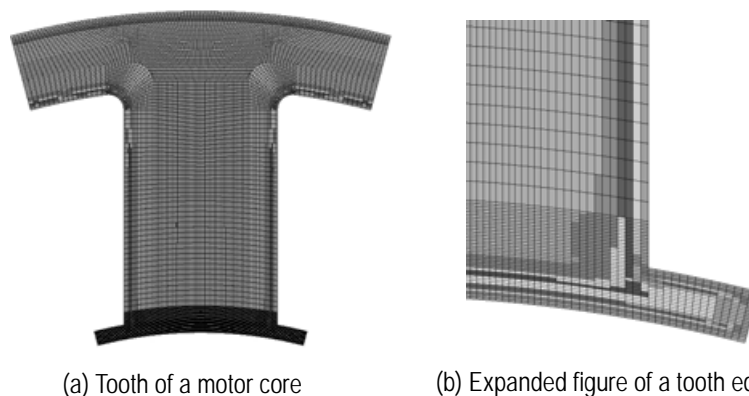(b) Expanded figure of a tooth edge

Fig. 4 FEM mesh, taking into account plastic strain and elastic stress distributions

the iron loss analysis were assumed to be no load and 3,000 rpm.

Figure 5(a) indicates that the effect of the strain and stress generated by the stamping alters the cogging torque. This is considered to occur as follows: the residual induction of the permanent magnet changes, which in turn changes the magnetic saturation condition inside the iron core, and thus the magnetic flux density in the gap changes. Figure 5(b) indicates that the effect of stamping increases the iron loss by about 1.6 times. In addition, from Fig. 5(c) as the residual induction of the permanent magnet increases, the increasing rate of the eddy current loss increases, whereas the increasing rate of the hysteresis loss decreases. This is considered to be an effect of the stamping process, which has changed the distribution of the magnetic flux density inside the iron core.

5. Conclusion

This paper discussed the quantitative effects of the stamping process on the cogging torque and iron loss of the permanent magnetic motor. The newly developed design technology makes it possible to accurately predict the product performance taking into consideration the magnetic property deterioration in mass production. We will verify the validity of this design technology for developing high-performance Mitsubishi motors.

Part of this study was conducted under the project "Development of High-Performance Battery System for Next-Generation Vehicles" commissioned by the New Energy and Industrial Technology Development Organization (NEDO).

References
(1) Akihiro, D., et al: Motor Design Technologies Considering Detailed Magnetic Properties in Magnetic Core, Mitsubishi Electric ADVANCE Vol. 116 5-7 (2006).
(2) Yamaguchi, S., et al.: Accurate Magnetic Field Analysis for Estimating Motor Characteristics Taking Account of Elasto-Plastic Deformation in the Magnetic Core, COMPUMAG (2009).
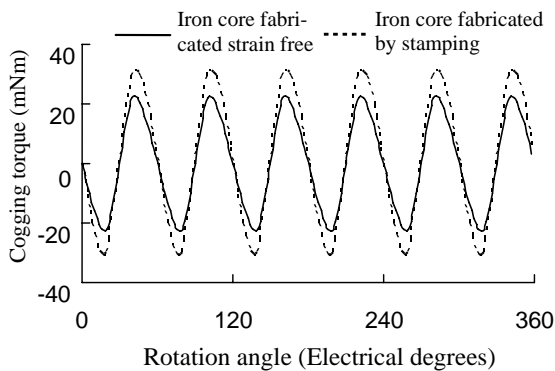
(a) Cogging torque (Residual induction of permanent magnet: 1.4 T)
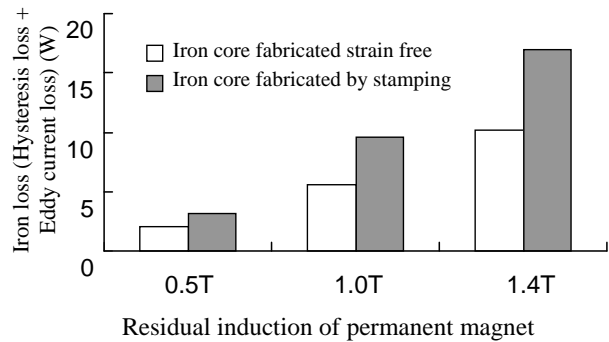
(b) Iron loss vs. Residual induction of permanent magnet
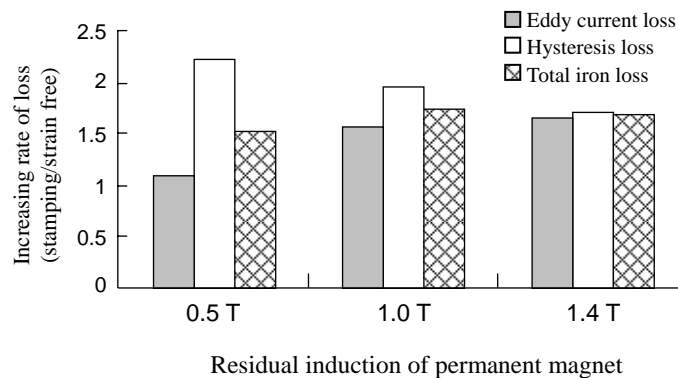
(c) Increasing rate of iron loss

Fig. 5 Calculated results of motor characteristics considering deteriorated magnetic properties in a magnetic core due to stamping

Estimation of Lateral Disturbance with Observer and Compensation Control with Electric Power Steering

Authors: *Hiroaki Kitano** and *Takanori Matsunaga***

When a car is traveling straight and a sudden crosswind or other lateral disturbance occurs, the car may slide sideways against the driver's will. Mitsubishi Electric has developed a technique to estimate and control lateral disturbance exerted on a car while driving straight, with a reduced computational load and by using standard sensors installed on board.

1. Estimation Method for Lateral Disturbance

If a crosswind occurs while a vehicle is traveling straight, lateral and rotational motions of the vehicle may occur against the driver's will. Mitsubishi Electric has modeled the effect of crosswind on the vehicle behavior and developed a new technique to estimate the lateral disturbance using a lateral disturbance observer. This paper describes the principle of this estimation.

Here, we examine the lateral and rotational motion of the vehicle based on the two-wheeled model,[1] which has the minimum computable degrees of freedom.

If a crosswind occurs while a vehicle is traveling straight, a lateral force and moment are exerted on the vehicle. We have designed a lateral disturbance observer based on the two-wheeled model of the vehicle to estimate the lateral disturbance using the information from sensors on board.[2] Vehicle control is then performed based on the estimated lateral disturbance to improve the straight traveling performance.

Figure 1 shows the outline of this control system.

Steering action by the driver is entered into the vehicle and reflected in the vehicle's behavior. The vehicle's behavior is then entered, as onboard sensor signals, into the lateral disturbance observer. From the entered signals, the observer estimates the amount of lateral disturbance, which is in turn converted to a compensation torque and superimposed on the assist torque of the electric power steering (EPS) to improve the straight traveling performance, canceling out the effect on the vehicle behavior caused by the lateral disturbance.
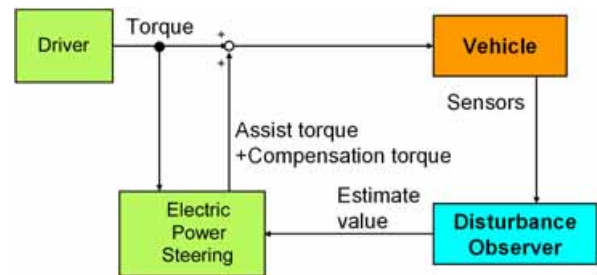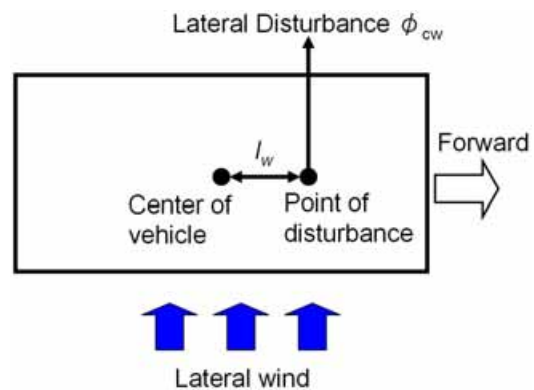

Fig. 1 Control system

Fig. 2 Disturbance model

A conventional lateral disturbance observer has been reported (Observer 1),[3] where the vehicle's center of gravity is assumed to coincide with the point of application of the lateral disturbance, and the moment Φ_{mo} due to the lateral disturbance is not considered. With this observer, however, an estimation error might arise due to disregarding the lateral disturbance moment.

Another method has also been reported (Observer 2),[2] where the moment of the lateral disturbance is taken into consideration in the above-described lateral disturbance observer. This method is thus able to accurately estimate the amount of lateral disturbance. However, the model becomes complicated, resulting in high computational load.

We have reduced the computational load by defining l_w as the distance between the point of application of the lateral disturbance on the vehicle (aerodynamic center) and the vehicle's center of gravity, and then determining the moment of the lateral disturbance, Φ_{mo}, from the lateral force of the lateral disturbance (New

observer).

Based on the estimation from the lateral disturbance observer, the electric power steering is controlled to generate an assist torque for facilitating straight traveling.

2. Simulation of Straight Traveling Control

Assuming a driver driving straight at a speed of 80 km/h without holding the wheel and the occurrence of a stepwise crosswind of 20 m/s, five seconds of driving was simulated.

Figure 3 shows the traveling path without the straight traveling control. Due to the lateral disturbance, lateral and rotational motions of the vehicle occur, resulting in 3.5 m of drifting toward downwind while traveling a distance of 100 m (for a duration of 4.5 s).

Figure 4 shows the traveling path controlled with the lateral disturbance Observer 1 by Ohta et al. An estimation error in the lateral force of the lateral disturbance, Φ_{cw}, generates an excessive compensation torque for straight traveling, resulting in more than 5 m of drifting in the opposite direction toward upwind while traveling a distance of 100 m.

Figures 5 and 6 show the traveling paths controlled

for straight traveling by the estimation, respectively, with Observer 2 and the newly developed lateral disturbance observer. Although there is a slight drift toward downwind due to a delay in initial estimation, the drift toward downwind is controlled to within 1 m while traveling a distance of 100 m, confirming an improvement in the straight traveling performance against the lateral disturbance.

It has been demonstrated that the new lateral disturbance observer reduces the computational load as well as improves the straight traveling performance against lateral disturbance to a level equivalent to or better than the lateral disturbance Observer 2.

References

(1) Abe, M.: "Motion of automotives and control – theory formation and application of vehicle kinetics", Tokyo Denki University Press, 2008 (Chapter 3).
(2) Tajima, K., Ohta, T., Suzuki, Y., and Ishige, T.: Japanese patent laid-open No. 2005-239012, 2005.
(3) Ohta, T., Mimuro, T., Lee, J.: "Robust Lateral Control System with Steering Torque Assist", Advanced Vehicle Control, 2002.
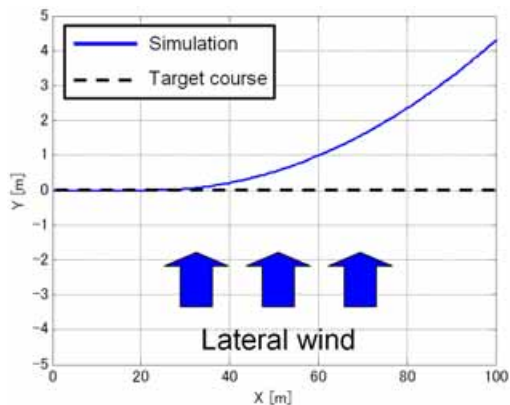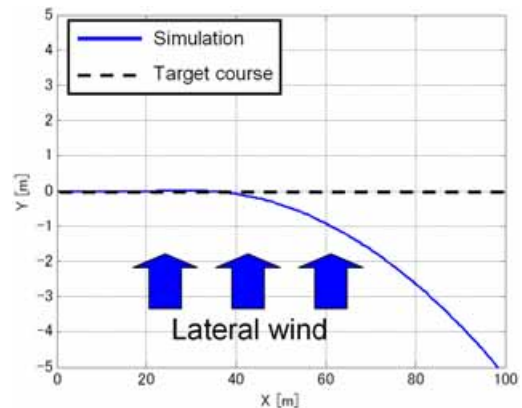
Fig. 3 Without control
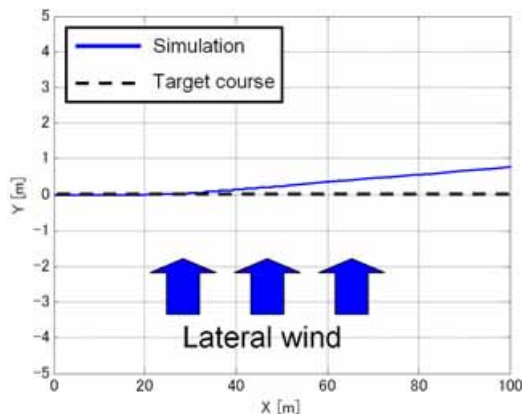
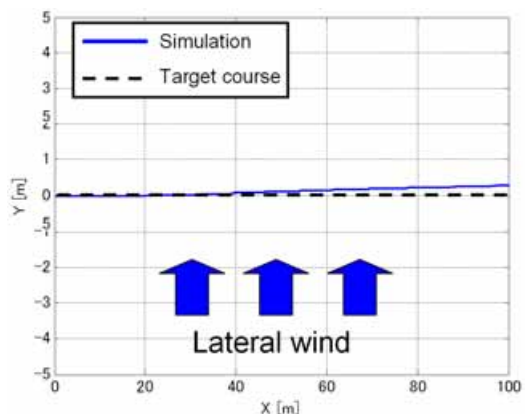Fig. 4 Control with observer 1

Fig. 5 Control with observer 2

Fig. 6 Control with proposed observer

Dynamic Simulation of Rope for High-speed Elevators

Authors: *Seiji Watanabe** and *Tsunehiro Higashinaka***

1. Introduction

Recently, many large earthquakes have hit Japan. When an earthquake occurs in a big city, many elevators are stopped by earthquake emergency operation. This makes it difficult for a long time for building residents to move up and down, causing inconvenience after an earthquake. Therefore, a seismic-resistant design for elevator systems is important for maintaining vertical transportation.

Damage prevention against long-period seismic ground motion is another important issue for high-speed elevators in high-rise buildings. When a strong earthquake occurs, the ground acceleration at a site far from the epicenter may not be sufficiently high to trigger seismic detectors. However, the sway of tall buildings increases, and elevator ropes resonate with the building motion. Lateral rope vibration may then cause entanglement in the elevator shaft or damage to shaft devices. To prevent damage due to long-period ground motion, new technologies based on transient analysis of buildings and ropes are being developed. This paper describes a new detector and special emergency operation to suppress lateral rope vibration.

2. Modeling of Building and Rope

The building is modeled as a multi-mass and spring system to evaluate the sway motion due to an earthquake. Each floor is represented by a dense mass, which is connected by a spring with shear stiffness between the floors, as shown in Fig. 1.

The first natural swing period T [s] is given by:

$$T = 0.025 \times H \qquad \cdots\cdots (1)$$

where H [m] is the building height.

Figure 2 shows the basic configuration of a high-speed elevator installed in a high-rise building. The elevator system contains many kinds of rope.

As the rope sway motion is evaluated by string vibration constrained at both ends, equations of motion of each rope are derived by a multi-mass and spring system as shown on the right side of Fig. 2.

3. Suppression of Lateral Rope Motion

When a strong earthquake occurs, a plain that is over 150 km away from the epicenter may suffer ground resonance, and continue to shake for as long as a 4- to 7-second period. If the site is far from the epicenter, the ground motion and acceleration are not sufficiently high to trigger seismic detectors. However, the sway of tall buildings increases, and then elevator ropes and cables are also affected by the long-period ground motion. If the rope resonates with the building
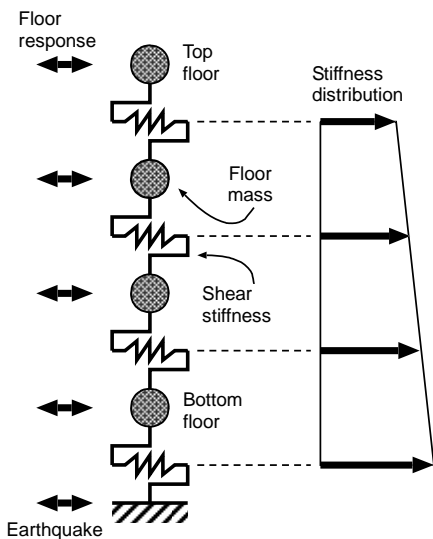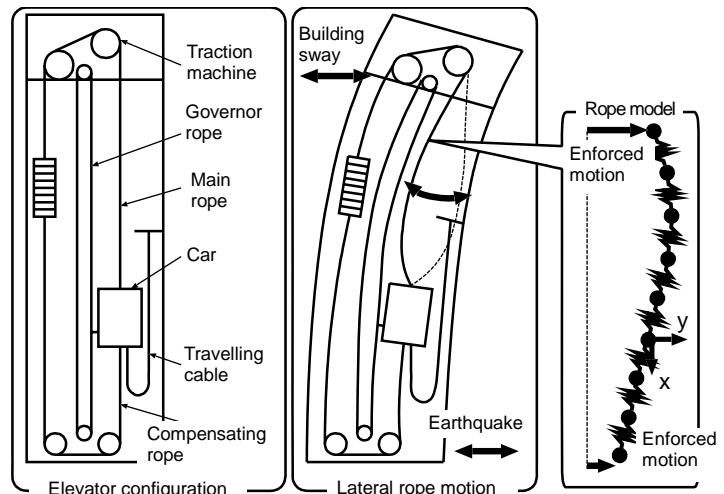

Fig. 1 Building model

Fig. 2 Configuration of elevator rope system

swaying motion, lateral rope vibration may cause entanglement in the elevator shaft or damage to shaft devices.

To prevent these problems, two ways to suppress lateral rope vibration are proposed: rope protectors in the shaft, and special emergency operation for long-period ground motion.

The elevator shaft contains many devices that might trap a swaying rope. Figure 3 shows the rope protector and tie-bar. These not only prevent rope entanglement, but also reduce the amplitude of rope sway motion, as shown in Fig. 4.

When a car stops at a certain floor, building sway motion causes lateral rope vibration as shown in Fig. 3.

Low acceleration with low frequency is difficult to measure by conventional seismic detectors. To detect such low acceleration, we developed a new detector for long-period ground motion. It contains two servo-type accelerometers to measure two horizontal directions, and then calculates the vector as building vibration. In addition to measuring building acceleration, it can also estimate lateral rope vibration simultaneously by using a simple rope model.

If the estimated rope vibration exceeds a preset level, the detector sends a signal to the elevator to switch the service to the special operation for long-period ground motion. The emergency operation contains three steps depending on the detector output as follows:

[LEVEL 0]

The system starts calculating lateral rope displacement due to a small acceleration trigger.

[LEVEL 1]

If the estimated rope displacement is over LEVEL 1, the car moves to the nearest floor and then stops.

[LEVEL 2]

If the estimated rope displacement is over LEVEL 2, the car stays at the floor until a manual check by a maintenance worker. If there is no LEVEL 2 trigger, then the car moves to a special floor, at which no ropes resonate with building vibration, as shown in Fig. 5.

If the car moves to a floor without rope resonance, the elevator can return to normal operation after the building vibration has settled. The emergency operation thus efficiently prevents damage to the rope and shaft devices.

4. Conclusion

The seismic motions of high-speed elevators installed in high-rise buildings are evaluated by simulation models, and new seismic technologies for long-period ground motion are introduced. At sites far from the epicenter of an earthquake, emergency operation for long-period ground motion can prevent damage inside the shaft due to lateral rope vibration.
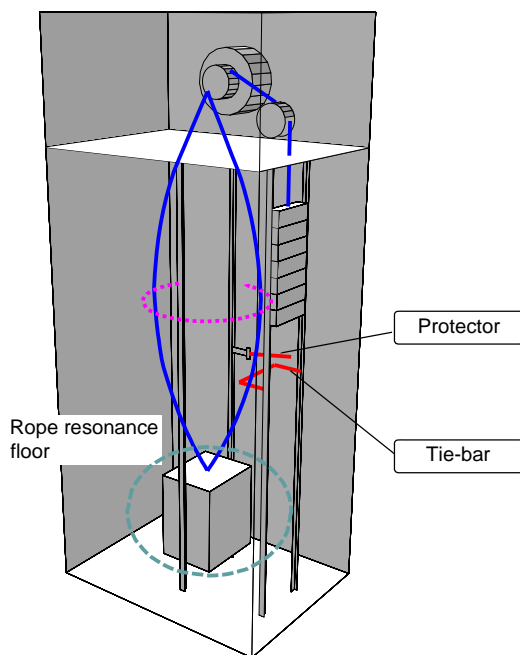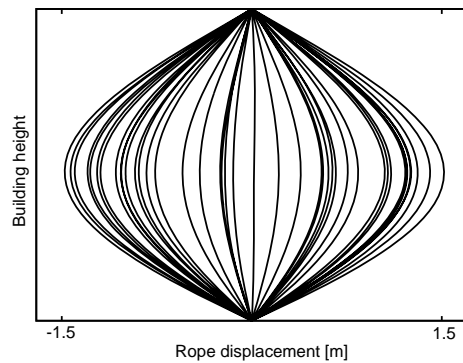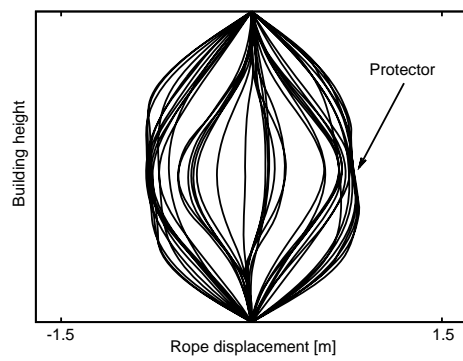

Fig. 3 Rope protection

(a) Without protector

(b) With protector
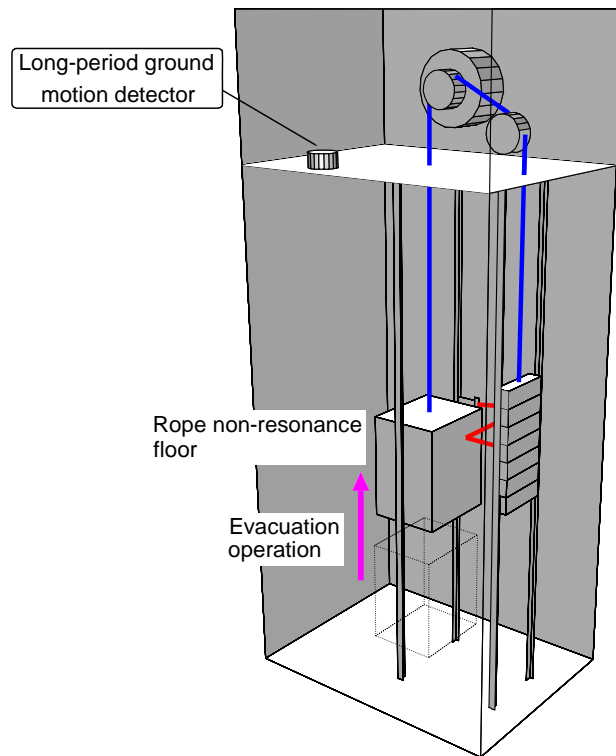
Fig. 4 Suppression of lateral rope motion

Fig. 5 Emergency operation

MITSUBISHI ELECTRIC CORPORATION